

Intercorrelated anomalous Hall and spin Hall effect in kagome-lattice $\text{Co}_3\text{Sn}_2\text{S}_2$ -based shandite films

Yong-Chang Lau,^{1,2,3,*} Junya Ikeda,¹ Kohei Fujiwara,¹ Akihiro Ozawa,¹ Takeshi Seki,^{1,2,†} Kentaro Nomura,^{1,2} Atsushi Tsukazaki,^{1,2,4,‡} and Koki Takanashi^{1,2,4}

¹*Institute for Materials Research, Tohoku University, Sendai 980-8577, Japan*

²*Center for Spintronics Research Network, Tohoku University, Sendai 980-8577, Japan*

³*Institute of Physics, Chinese Academy of Sciences, Beijing 100190, China*

⁴*Center for Science and Innovation in Spintronics,*

Core Research Cluster, Tohoku University, Sendai 980-8577, Japan

(Dated: March 7, 2022)

Magnetic Weyl semimetals (mWSMs) is characterized by linearly dispersive bands with chiral Weyl node pairs associated with broken time reversal symmetry. One of the hallmarks of mWSMs is the emergence of large intrinsic anomalous Hall effect. On heating the mWSM above its Curie temperature, the magnetism vanishes while exchange-split Weyl point pairs collapse into doubly-degenerated gapped Dirac states. Here, we reveal the attractive potential of these Dirac nodes in paramagnetic state for efficient spin current generation at room temperature via the spin Hall effect. Ni and In are introduced to separately substitute Co and Sn in a prototypal mWSM $\text{Co}_3\text{Sn}_2\text{S}_2$ shandite film and tune the Fermi level. Composition dependence of spin Hall conductivity for paramagnetic shandite at room temperature resembles that of anomalous Hall conductivity for ferromagnetic shandite at low temperature; exhibiting peak-like dependence centering around the Ni-substituted $\text{Co}_2\text{Ni}_1\text{Sn}_2\text{S}_2$ and undoped $\text{Co}_3\text{Sn}_2\text{S}_2$ composition, respectively. The peak shift is consistent with the redistribution of electrons' filling upon crossing the ferromagnetic-paramagnetic transition, suggesting intercorrelation between the two Hall effects. Our findings highlight a novel strategy for the quest of spin Hall materials, guided by the abundant experimental anomalous Hall effect data of ferromagnets in the literature.

Non-trivial topology in the band structure of a solid can give rise to large Berry curvature [1, 2] acting as an effective magnetic field in real space. This field can deflect the electrons in motion, leading to an intrinsic off-diagonal transport contribution that does not depend on the extrinsic electrons' scattering rate. Typical examples are the anomalous Hall effect (AHE) [3] in ferromagnets and its spin counterpart the spin Hall effect (SHE) [4]. The latter often involves non-magnetic metals with strong spin-orbit coupling and allows generation of a transverse spin current capable of manipulating the magnetization of an adjacent nanomagnet. The resulting spin-orbit torques (SOT) [5] is promising for applications including non-volatile memory, magnetic logic, field sensing and neuromorphic computing. Finding material systems that exhibit high charge-to-spin conversion efficiency is a key to realize competitive spin-orbitronic devices with low power consumption.

SHE has thus far only been investigated for a small subset of all the known materials. One primary challenge for probing the SHE is the non-conservative nature of the spin current, thus necessitates material integration into devices of comparable length scale (e.g., the thickness) with the commonly nanometric spin diffusion length λ [6]. In contrast, owing to its ease of evaluation and prolonged history, the AHE for many conducting magnetic materi-

als are known and available in the literature. In view of the very similar origin and scaling relationship for AHE [7] and SHE [8], it is tempting to study the intercorrelation between them. Using the abundant AHE data as a facile indicator, one may unveil new design principles for materials with large SHE. Different from the trivial electronic bands in conventional 3d ferromagnetic metals [9], we focus on one of the topological bands in a magnetic Weyl semimetal (mWSM) [10–13] prototype cobalt shandite $\text{Co}_3\text{Sn}_2\text{S}_2$ (CSS) to reveal the intriguing correlation between the AHE and SHE.

Figure 1(a) illustrates a rhombohedral structure of CSS (Space group No. 166; $R\bar{3}m$) which consists of alternate $\text{Co}_3\text{Sn}/\text{SnS}_2$ planes, stacking along the \mathbf{c} -axis in the hexagonal representation. Co atoms form a kagome lattice within the \mathbf{ab} plane and exhibit strong perpendicular magnetic anisotropy with Curie temperature (T_C) of $\sim 177\text{K}$. Recent spectroscopic studies [14, 15] have established ferromagnetic CSS (FM-CSS) as an exotic mWSM with pairs of Weyl points (WPs) near the Fermi level (E_F) connected by the chiral surface Fermi arcs. This leads to large summation of the Berry curvature in FM-CSS, exhibiting a record-high anomalous Hall angle exceeding 0.2 [16, 17]. The relatively low T_C of CSS, however, hinders the prospect of exploiting its topological properties for many practical applications. So far, very limited studies [18] were devoted to explore the usefulness of paramagnetic CSS (PM-CSS) at room temperature. Here, we highlight the intercorrelation between the intrinsic AHE and SHE for CSS-based compounds, across the ferromagnetic-paramagnetic transition. We

* yongchang.lau@iphy.ac.cn

† takeshi.seki@tohoku.ac.jp

‡ tsukazaki@tohoku.ac.jp

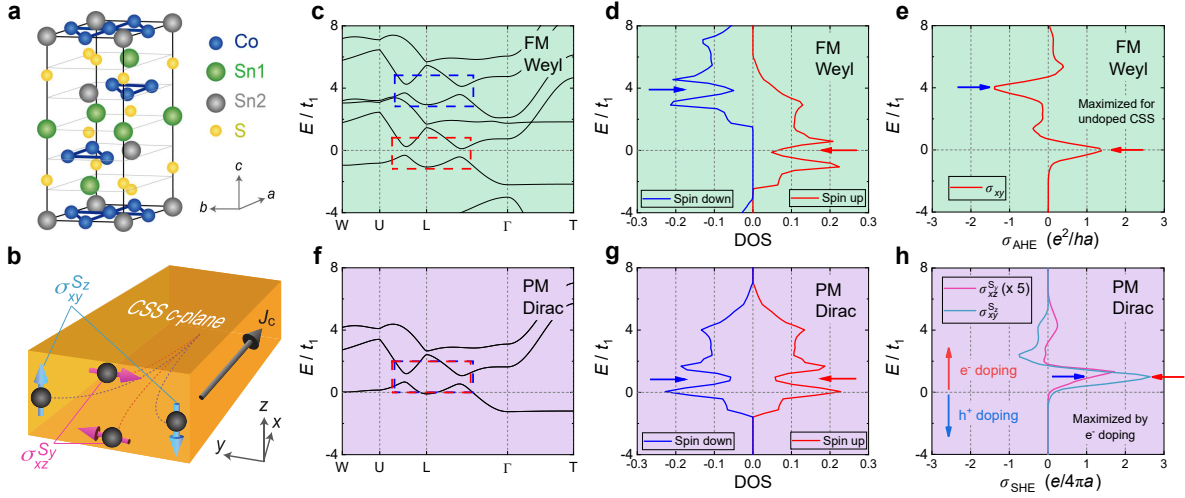


FIG. 1. (a) Unit cell of $\text{Co}_3\text{Sn}_2\text{S}_2$ with a Co-kagome lattice in the (ab) plane (hexagonal representation). (b) Passing a charge current j_c within the kagome plane along \mathbf{x} generates, via the spin Hall effect, an orthogonal spin current of conductivity $\sigma_{xy}^{S_z}$ ($\sigma_{xz}^{S_y}$) that flows along \mathbf{y} (\mathbf{z}) with polarization along \mathbf{z} (\mathbf{y}). (c-e) Calculated electronic band structure (c), spin-resolved density of states (DOS) (d), and anomalous Hall conductivity σ_{xy} (e) as a function of Fermi energy for ferromagnetic (FM) $\text{Co}_3\text{Sn}_2\text{S}_2$ in the magnetic Weyl semimetal state. (f-h) Calculated electronic band structure (f), spin-resolved DOS (g), and two selected components $\sigma_{xy}^{S_z}$ and $\sigma_{xz}^{S_y}$ of the spin Hall conductivity tensor (h) for paramagnetic (PM) $\text{Co}_3\text{Sn}_2\text{S}_2$. $E/t_1 = 0$ represents the Fermi level E_F for undoped $\text{Co}_3\text{Sn}_2\text{S}_2$ in the FM and PM states, respectively. Red and blue dashed boxes in (c) and (f) represent the position of the Weyl/Dirac points. The arrows in (d), (e), (g), and (h) indicate contributions of these Weyl/Dirac points in DOS and Hall conductivities.

further demonstrate that Fermi-level tuning via isostructural substitutional alloying is an effective strategy allowing full exploitation of the topological features in the band structure of PM-CSS, for efficient spin current generation via SHE at room temperature.

To elucidate our concept, we consider a two-orbital effective tight-binding model of CSS [19, 20]. A longitudinal charge current j_c is applied along \mathbf{x} in the \mathbf{ab} kagome plane, as illustrated in Fig. 1(b). The magnetization is along \mathbf{z} coinciding with the \mathbf{c} -axis. We first focus on FM-CSS in the mWSM state, corresponding to Figs. 1(c)–1(e). Highlighted by the dashed red box in the simplified electronic band structure of half-metallic FM-CSS in Fig. 1(c), the two WPs in the vicinity of E_F (represented by $E/t_1 = 0$), manifest themselves in the spin-resolved density of states (DOS) [Fig. 1(d)] as a minima of the majority spin-up DOS. The anomalous Hall conductivity σ_{xy} (AHC) [Fig. 1(e)] exhibits a peak centering around the WPs at E_F . We highlight that at higher energy, a similar σ_{xy} peak of opposite sign appears (blue arrow), which is attributed to the two conjugated WPs from the spin-down bands [Fig. 1(c); dashed blue box]. Using the lattice parameter of CSS $a = 0.538 \text{ nm}$ and recognizing e^2/h is half of the conductance quantum, at E_F , we obtain $\sigma_{xy} \approx 1.0 \times 10^3 \Omega^{-1} \text{ cm}^{-1}$, which agrees with the experiment and first-principles calculations [16].

The calculated properties for PM-CSS where the exchange splitting is absent are shown in Figs. 1(f)–1(h). The conjugated WPs annihilate into doubly-degenerated Dirac points followed by gap opening due to spin-orbit

coupling. [Fig. 1(f); dashed boxes] [21, 22] The spin-resolved DOS of the two spins channels are equal, as shown in Fig. 1(g). σ_{xy} vanishes because contributions from the two spins exactly cancel each other, as expected for a paramagnet. In contrast, the spin current is time reversal invariant, e.g., a spin-up spin current flowing along \mathbf{y} is equivalent to a spin-down spin current flowing along $-\mathbf{y}$. The spin Berry curvature contributions from the two spin channels are additive and linked to the position of the gapped Dirac point. As depicted in Fig. 1(b), for j_c along \mathbf{x} , we define the spin Hall conductivity (SHC) $\sigma_{xi}^{S_j}$ ($i, j = x, y, z$) where the spin current is flowing along \mathbf{i} with polarization along \mathbf{j} . Lateral SHC $\sigma_{xy}^{S_z}$ [Fig. 1(h); skyblue] of approximately twice-as-large to AHC is expected near the gapped Dirac point. Using the same a , we obtain $\sigma_{xy}^{S_z} \approx 1.9 \times 10^3 (\hbar/2e)\Omega^{-1} \text{ cm}^{-1}$, which approaches that of a typical spin Hall metal Pt [23, 24]. In practice, for (0001)-textured CSS film in this work, it is more convenient to detect the spin current flowing along \mathbf{z} with polarization along \mathbf{y} , i.e., $\sigma_{xz}^{S_y}$. Calculations suggest a peak near the gapped Dirac point for $\sigma_{xz}^{S_y}$ [Fig. 1(h); pink]. This maximum is however smaller than that of $\sigma_{xy}^{S_z}$ where charge and spin current are both flowing in the kagome plane, a feature resembles another kagome semimetal Fe_3Sn_2 with highly anisotropic AHC tensor [25]. The strong anisotropy reflects that the interplay between the conduction electron, kagome lattice, and spin-orbit coupling determines the Hall effects. We emphasize that SHC of undoped PM-CSS is unoptimized

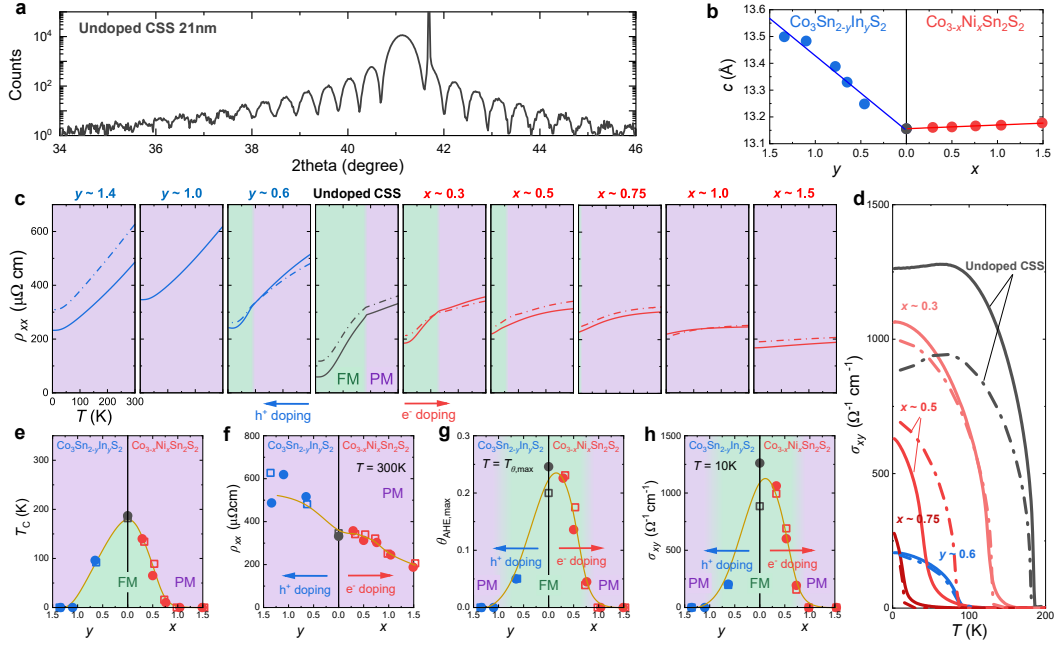


FIG. 2. (a) Typical x-ray diffraction spectrum for an undoped $\text{Co}_3\text{Sn}_2\text{S}_2$ shandite film showing clear Laué fringes near the $\text{Co}_3\text{Sn}_2\text{S}_2(0006)$ reflection. (b) Ni composition x and In composition y dependence of out-of-plane lattice parameter c deduced from the peak position of the (0006) reflection. (c, d) Temperature T dependence of the longitudinal resistivity ρ_{xx} (c) and anomalous Hall conductivity σ_{xy} (d) for shandite films of various x and y . Solid and dashed lines represent data for the films before and after removing the thick SiO_x capping, respectively. (e-g) x and y dependence of the Curie temperature T_C (e), ρ_{xx} at $T = 300$ K (f), the maximum anomalous Hall angle $\theta_{\text{AHE,max}} \equiv \sigma_{xy}\rho_{xx}$ extracted at $T = T_{\theta,\text{max}}$ (g), and σ_{xy} at 10 K (h). Solid and open symbols denote data for shandite films before and after removing the thick SiO_x capping, respectively. Dark yellow solid lines are drawn for guides to the eye.

as E_F is well below the gapped Dirac point. Within rigid band approximations, an electron doping of ~ 1 electron per formula unit is required to reposition E_F close to the gapped Dirac point, for which a dramatic enhancement of SHC is expected.

We have grown textured undoped CSS, Ni-substituted $\text{Co}_{3-x}\text{Ni}_x\text{Sn}_2\text{S}_2$ (CNSS), and In-substituted $\text{Co}_3\text{Sn}_{2-y}\text{In}_y\text{S}_2$ (CSIS) films with thicknesses ranging from 11 to 40 nm on $\text{Al}_2\text{O}_3(0001)$ substrates by co-sputtering as described previously and in Section S1 of the Supplemental Material [20, 26–28]. x and y denote the composition of Ni and In, respectively. Upon replacing Co with Ni (Sn with In), the electron (hole) doping is expected to shift E_F to higher (lower) energies. The crystal structure of CSS is maintained throughout because CSS, $\text{Ni}_3\text{Sn}_2\text{S}_2$ and $\text{Co}_3\text{In}_2\text{S}_2$ are isostructural compounds. Figure 2(a) shows typical x-ray diffraction (XRD) spectrum for an undoped CSS film exhibiting clear Laué fringes around the CSS (0006) reflection, indicative of strong (0001) texture with sharp interfaces. In-plane XRD Φ scan of the CSS $(11\bar{2}0)$ reflection, however, shows peaks that are 30° apart, reflecting the presence of in-plane twinned domains. The out-of-plane lattice parameter c in Fig. 2(b) was extracted from the (0006) peak position and suggests systematic tuning of x and y .

The magneto-transport as a function of temperature T in Figs. 2(c) and 2(d) provides another evidence of systematic tuning of film properties by alloying. Solid lines denote data for undoped CSS (black), CNSS (red) and CSIS (blue) films covered by a thick ~ 75 nm SiO_x protective layer, whereas dashed lines represent the data for samples after removing the SiO_x layer by Ar ion milling followed by the deposition of 3 nm AlO_x capping [20]. The high quality of our undoped CSS film gives rise to a residual resistivity ratio, $\text{RRR} \equiv \rho_{xx}(T = 300\text{K})/\rho_{xx}(T = 10\text{K}) \sim 3$. For doped films, the kink in ρ_{xx} reflecting T_C and the average resistance are systematically controlled by In and Ni contents. Meanwhile, σ_{xy} [Fig. 2(d)] is nearly a plateau for T sufficiently far below T_C , suggesting the intrinsic nature of the AHE. T_C , ρ_{xx} at $T = 300$ K, the maximum anomalous Hall angle $\theta_{\text{AHE,max}} \equiv \sigma_{xy}\rho_{xx}$ at $T = T_{\theta,\text{max}}$, and σ_{xy} at 10 K are summarized in Figs. 2(e)–2(h). Referring to Stoner criterion, both electron and hole doping reduce T_C because E_F of undoped PM-CSS falls on a local maxima of the DOS [Fig. 1(g)]. Similarly, σ_{xy} at 10 K and $\theta_{\text{AHE,max}}$ are maximized for undoped FM-CSS and fall rapidly with increasing x and y . These observations confirm the correlation between the large intrinsic σ_{xy} and the E_F positioning relative to the magnetic WPs.

We next fabricate undoped $\text{CSS}(t)/\text{Cu}(1.8)/\text{CoFeB}(2)$

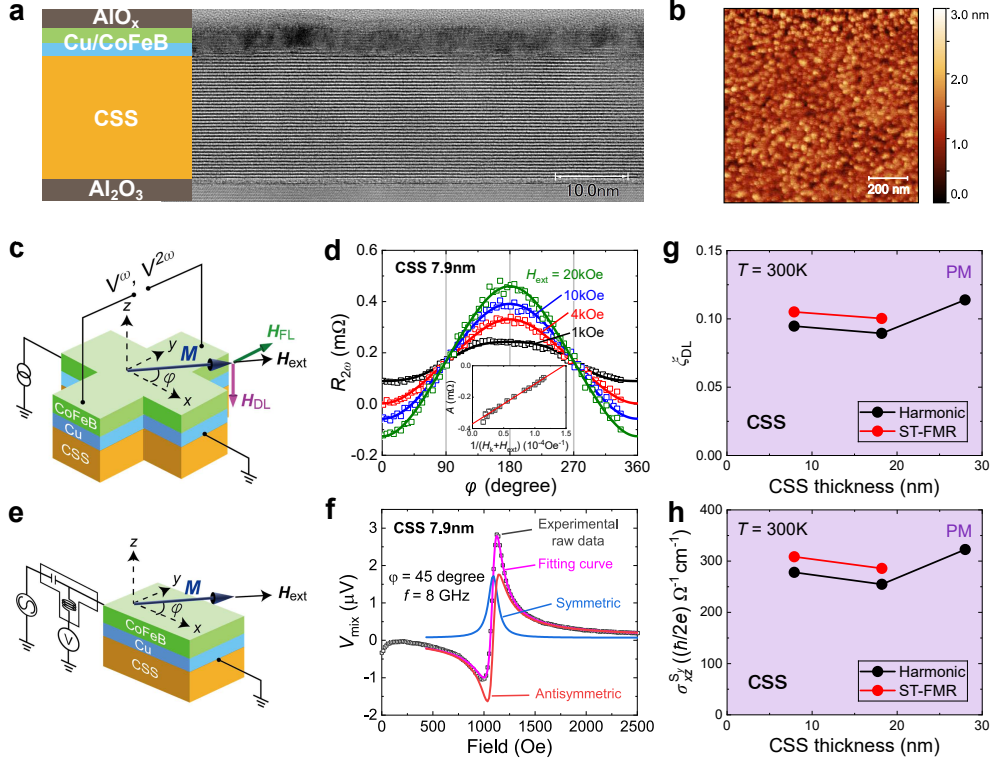


FIG. 3. (a) A schematic of the stack structure and high-resolution cross sectional transmission electron microscopy image for a trilayer with $\text{Co}_3\text{Sn}_2\text{S}_2$ (CSS) thickness $t = 18.5$ nm. (b) Atomic force microscopy image for a trilayer with $t = 7.9$ nm, showing a low root mean square roughness of ~ 0.3 nm. (c-f) Spin-orbit torque quantification of $\text{Co}_3\text{Sn}_2\text{S}_2$ (7.9)/Cu/CoFeB trilayers at $T = 300$ K. Schematic illustration of the harmonic Hall measurement set-up (c) and azimuthal field angle φ dependence of the second harmonic Hall resistance $R_{2\omega}$ (d) measured at various external fields H_{ext} . Inset of (d) plots A , the prefactor of the $\cos \varphi$ term of $R_{2\omega}$ against the inverse of the effective field $1/(H_k + H_{\text{ext}})$ (10^4Oe^{-1}). Red line is the best linear fit to the data. Schematic illustration of the spin-torque ferromagnetic resonance (ST-FMR) measurement set-up (e) and a typical FMR spectrum (f) measured at 8 GHz with an applied field along $\varphi = 45^\circ$. The fit and decomposition of the spectrum is based on the sum of a symmetric and an antisymmetric Lorentzian [20]. (g-h) t dependence of the damping-like spin Hall efficiency ξ_{DL} (g) and spin Hall conductivity $\sigma_{xz}^{S_y}$ (h).

(thicknesses in nanometer) trilayers [See Supplemental Material [20]] for investigating the charge-to-spin conversion at $T = 300$ K, i.e., when CSS is paramagnetic. t denotes the thickness of the CSS layer. Figure 3(a) shows a typical high-resolution cross sectional transmission electron microscopy (HR-TEM) image of CSS(18.5)/Cu(1.8)/CoFeB(2) trilayer where the layered structure of high-quality CSS is clearly visible. The average grain size of CSS (> 50 nm) is significantly larger than that of Cu/CoFeB (~ 10 nm). Energy dispersive x-ray spectroscopy (EDX) mapping confirms that all layers of the heterostructure are continuous with limited interdiffusion [See Fig. S1 in Supplemental Material [20]]. Typical atomic force microscopy (AFM) micrograph [Fig. 3(b)] of the trilayer for $t = 7.9$ nm reveals flat surface morphology with a low root mean square (r.m.s.) surface roughness of ~ 0.3 nm, which is a prerequisite for spintronic device integration in the future.

On passing a charge current along \mathbf{x} , CSS generates a spin current flowing along \mathbf{z} that traverses the Cu

spacer and exerts SOTs on the CoFeB with in-plane magnetization. Limited by the thin film geometry, only $\sigma_{xz}^{S_i}$; $i = x, y, z$ are accessible. The thin Cu spacer with long λ physically separates CSS and CoFeB, thus avoiding local enrichment of Co at the interface which may alter the properties of CSS. The observation of $\sim 1\%$ current-in-plane giant magnetoresistance for the trilayer at $T = 50$ K (i.e., when CSS is ferromagnetic) confirms the finite spin transparency across the Cu spacer [See Fig. S2 in Supplemental Material [20]]. We first employ the harmonic Hall technique [29, 30] to quantify the damping-like and field-like spin-orbit effective fields (H_{DL} and H_{FL} , respectively) acting on the CoFeB magnetization [Fig. 3(c)]. The dependence of second harmonic Hall resistance $R_{2\omega}$ on the external field H_{ext} and its azimuthal angle φ allows separation of the SOT contribution ($\propto \frac{1}{H}$) from the parasitic thermoelectric effects [31–33]. Figure 3(d) plots the φ -dependence of $R_{2\omega}$ measured at various H_{ext} for trilayer with $t = 7.9$ nm and a current density flowing in the CSS of $j_{\text{CSS}} \sim$

$1.6 \times 10^6 \text{ A cm}^{-2}$. $R_{2\omega}(\varphi)$ is dominated by the $\cos \varphi$ term, defined with a prefactor A . [See Section S2 of the Supplemental Material for the detailed analysis of the harmonic Hall measurement [20]] H_{DL} is extracted by linear fitting A against the inverse of the effective in-plane field $1/(H_k + H_{\text{ext}})$ [insets of Fig. 3(d)]. We found $H_{\text{DL}}/j_{\text{CSS}} = 1.4 \times 10^{-6} \text{ Oe A}^{-1} \text{ cm}^2$, corresponding to a DL spin Hall efficiency $\xi_{\text{DL}} = \frac{2e}{\hbar} \frac{H_{\text{DL}} M_s t_{\text{CoFeB}}}{j_{\text{CSS}}} \approx +0.10$ where e is the elementary charge, \hbar the Planck constant, $M_s = 1200 \text{ emu cm}^{-3}$ the saturation magnetization, and $t_{\text{CoFeB}} = 2 \text{ nm}$ the CoFeB thickness. ξ_{DL} of undoped PM-CSS is of the same sign as that of Pt. Its absolute magnitude is larger than another mWSM prototype Co_2MnGa ($\xi_{\text{DL}} \sim -0.07$ in the ferromagnetic state) [34]. With $\rho_{xx} \approx 340 \mu\Omega \text{ cm}$, we obtained $\sigma_{xz}^{S_y} = \xi_{\text{DL}}/\rho_{xx} \approx 300(\hbar/2e)\Omega^{-1}\text{cm}^{-1}$.

For an independent verification, we performed spin-torque ferromagnetic resonance (ST-FMR) [set-up depicted in Fig. 3(e)] measurement [35] on microstripes fabricated on the same substrate. A representative FMR spectrum measured from the mixing voltage V_{mix} while applying H_{ext} along $\varphi = 45^\circ$ is shown in Fig. 3(f). Data is fitted by the sum of a symmetric and an antisymmetric Lorentzian. More details of the analysis can be found in the Section S3 of the Supplemental Material [20]. The emergence of an appreciable symmetric component (blue) confirms the generation of DL-SOT from the undoped PM-CSS at room temperature. Line-shape analysis taking into account current shunting in the Cu spacer yields $\xi_{\text{DL}} = +0.11$, in excellent agreement with the harmonic Hall results. The full φ dependence of ST-FMR confirms the dominant role of spin current with polarization along \mathbf{y} [See Fig. S4(a) in Supplemental Material [20]]. Figures 3(g) and 3(h) summarize the CSS thickness t -dependence of ξ_{DL} and $\sigma_{xz}^{S_y}$, obtained from the two techniques. The almost constant trend for ξ_{DL} and $\sigma_{xz}^{S_y}$ against t is consistent with bulk-like SHE and λ much shorter than $t = 7.9 \text{ nm}$.

We now extend the harmonic Hall SOT quantification at $T = 300 \text{ K}$ to Ni-substituted and In-substituted CSS/Cu/CoFeB trilayers. Contrary to σ_{xy} that is maximized for undoped FM-CSS, both ξ_{DL} and $\sigma_{xz}^{S_y}$ [Figs. 4(a) and 4(b)] exhibit a pronounced peak for electron-doped PM shandites. The highest $\xi_{\text{DL}} = +0.15$ is achieved for PM- $\text{Co}_{2.25}\text{Ni}_{0.75}\text{Sn}_2\text{S}_2$ ($x \sim 0.75$), showing a large controllability of one order of magnitude by the composition variation. Taking into account the conductivity enhancement on increasing x [Fig. 2(f)], the peak of $\sigma_{xz}^{S_y} \approx 500(\hbar/2e)\Omega^{-1}\text{cm}^{-1}$ is shifted to $\text{Co}_{2.02}\text{Ni}_{0.98}\text{Sn}_2\text{S}_2$ ($x \sim 1.0$). Both ξ_{DL} and $\sigma_{xz}^{S_y}$ decrease dramatically upon increasing Ni composition to $x \sim 1.5$ or introducing In for hole doping. A direct comparison of the harmonic Hall results for CNSS($x \sim 1.0$)/Cu/CoFeB trilayer and CSIS($y 0.6$)/Cu/CoFeB trilayer is shown in Fig. S3 in the Supplemental Material [20]. Compared to the $\theta_{\text{AHE,max}}$ and AHC (σ_{xy}) peaks near $x \sim 0$ for FM-CSS [Right axes and dark yellow lines in Figs. 4(a) and 4(b); repro-

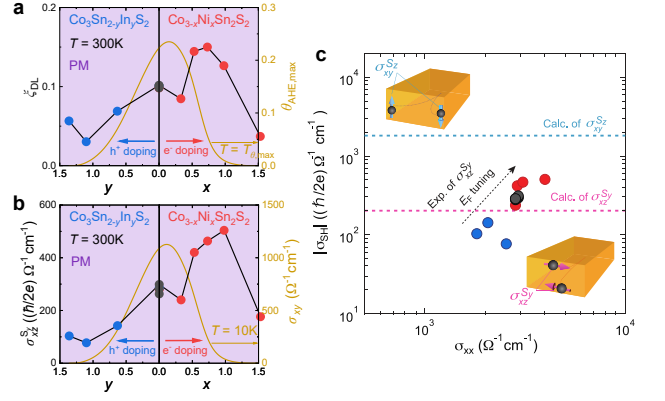


FIG. 4. (a,b) Nickel (Ni) composition x and Indium (In) composition y dependence of the damping-like spin Hall efficiency ξ_{DL} (a) and spin Hall conductivity $\sigma_{xz}^{S_y}$ (b), for paramagnetic shandites based on the harmonic Hall technique, measured at 300 K. Right axes and dark yellow lines show the maximum anomalous Hall angle $\theta_{\text{AHE,max}}$ and anomalous Hall conductivity σ_{xy} measured at low temperature. (c) $\sigma_{xz}^{S_y}$ against the longitudinal conductivity σ_{xx} for all the samples. The calculated spin Hall conductivity maxima for $\sigma_{xz}^{S_y}$ and $\sigma_{xy}^{S_z}$ are indicated by the dashed lines.

duced from Figs. 2(g) and 2(h)], the observed peak shifts in the composition dependence of ξ_{DL} and SHC ($\sigma_{xz}^{S_y}$) for PM-CSS agree with our calculations in Fig. 1. Since the conductivity of CNSS is in the "moderately dirty" regime, one may consider the intrinsic contribution dominates the SHC. The observed evolution of SHC against x and y thus mainly reflects the relative position between E_F and a source of spin Berry curvature in momentum space, e.g., a gapped Dirac point. The intercorrelation between the AHE and SHE shown here may constitute a transport signature of Weyl-Dirac topological transition in mWSM and the associated redistribution of the electron's filling [21, 22].

The experimental $\sigma_{xz}^{S_y}$, spanning over a factor of ~ 5 , is plotted against the longitudinal conductivity σ_{xx} and compared with the calculated $\sigma_{xz}^{S_y}$ and $\sigma_{xy}^{S_z}$ maxima [horizontal dashed lines] in Fig. 4(c). We consider mis-oriented CSS/Cu interface and other extrinsic mechanisms [36] may result in experimental $\sigma_{xz}^{S_y}$ that exceeds the calculated maximum. More interestingly, the highly anisotropic SHC tensor inherit from the CSS kagome lattice may allow further SHC enhancement, provided high-quality shandite films with c -axis lying in the film plane can be stabilized.

Compared to AHE which can be easily measured for a slab-shape ferromagnetic sample of any size, observation and quantification of SHE is far more challenging, rendering its vast screening laborious and unrealistic. Here, we have demonstrated a strategy where the large intrinsic AHE of a ferromagnetic material may serve as a facile indicator for predicting new paramagnetic compounds with

potentially enhanced intrinsic SHE. This rule of thumb is best applied to ferromagnets where contribution from one spin channel dominates its intrinsic AHE and Berry curvature, as exemplified by the half-metallic mWSM $\text{Co}_3\text{Sn}_2\text{S}_2$. Another prototypical mWSM Co_2MnGa [37] belonging to the highly tunable full Heusler family [38] may also work, provided a proper dopant that simultaneously introduces additional electrons and reduces T_C can be identified. Reciprocally, introducing a ferromagnetic hole dopant into well-established paramagnetic spin Hall materials may lead to the discovery of new ferromagnets with large AHC. This may explain the recent demonstration of large AHC in L1_2 -ordered CrPt_3 compound [39]. One should however be cautious in view of the metallic nature of these materials and the strong spin-orbit coupling of Pt. As a final remark, this strategy is readily extendable to the material screening for thermoelectric

generation via the anomalous Nernst effect [40–42] and spin Nernst effect [43, 44], provided in addition the Mott relation [45] is satisfied.

ACKNOWLEDGEMENTS

The authors are grateful to T. Sasaki and T. Kubota for their help in the preparation of trilayer heterostructures. This work was supported by JSPS KAKENHI Grant-in-Aid for Scientific Research (S) (JP18H05246), Grant-in-Aid for Early-Career Scientists (Grant No. JP20K15156), Grant-in-Aid for Scientific Research (A) (JP20H00299), Grant-in-Aid for Scientific Research (B) (JP20H01830), and JST CREST (JPMJCR18T2). A.O was supported by GP-Spin at Tohoku University and by JST SPRING (Grant No. JPMJSP2114).

-
- [1] M. V. Berry, Quantal phase factors accompanying adiabatic changes, *Proceedings of the Royal Society of London. A. Mathematical and Physical Sciences* **392**, 45 (1984).
- [2] D. Xiao, M.-C. Chang, and Q. Niu, Berry phase effects on electronic properties, *Rev. Mod. Phys.* **82**, 1959 (2010).
- [3] N. Nagaosa, J. Sinova, S. Onoda, A. H. MacDonald, and N. P. Ong, Anomalous hall effect, *Rev. Mod. Phys.* **82**, 1539 (2010).
- [4] J. Sinova, S. O. Valenzuela, J. Wunderlich, C. H. Back, and T. Jungwirth, Spin hall effects, *Rev. Mod. Phys.* **87**, 1213 (2015).
- [5] A. Manchon, J. Železný, I. M. Miron, T. Jungwirth, J. Sinova, A. Thiaville, K. Garello, and P. Gambardella, Current-induced spin-orbit torques in ferromagnetic and antiferromagnetic systems, *Rev. Mod. Phys.* **91**, 035004 (2019).
- [6] J. Bass and W. P. Pratt, Spin-diffusion lengths in metals and alloys, and spin-flipping at metal/metal interfaces: an experimentalist’s critical review, *Journal of Physics: Condensed Matter* **19**, 183201 (2007).
- [7] S. Onoda, N. Sugimoto, and N. Nagaosa, Quantum transport theory of anomalous electric, thermoelectric, and thermal hall effects in ferromagnets, *Phys. Rev. B* **77**, 165103 (2008).
- [8] H. Moriya, A. Musha, S. Haku, and K. Ando, Observation of the crossover between metallic and insulating regimes of the spin hall effect, *Communications Physics* **5**, 12 (2022).
- [9] Y. Omori, E. Sagasta, Y. Niimi, M. Gradhand, L. E. Hueso, F. Casanova, and Y. Otani, Relation between spin hall effect and anomalous hall effect in 3d ferromagnetic metals, *Phys. Rev. B* **99**, 014403 (2019).
- [10] O. Vafek and A. Vishwanath, Dirac fermions in solids: From high- t_c cuprates and graphene to topological insulators and weyl semimetals, *Annual Review of Condensed Matter Physics* **5**, 83 (2014).
- [11] B. Yan and C. Felser, Topological materials: Weyl semimetals, *Annual Review of Condensed Matter Physics* **8**, 337 (2017).
- [12] N. P. Armitage, E. J. Mele, and A. Vishwanath, Weyl and dirac semimetals in three-dimensional solids, *Rev. Mod. Phys.* **90**, 015001 (2018).
- [13] N. Nagaosa, T. Morimoto, and Y. Tokura, *Topological Properties of Weyl Materials*, *Nature Reviews Materials* **5**, 621 (2020).
- [14] D. F. Liu, A. J. Liang, E. K. Liu, Q. N. Xu, Y. W. Li, C. Chen, D. Pei, W. J. Shi, S. K. Mo, P. Dudin, T. Kim, C. Cacho, G. Li, Y. Sun, L. X. Yang, Z. K. Liu, S. S. P. Parkin, C. Felser, and Y. L. Chen, Magnetic weyl semimetal phase in a kagomé crystal, *Science* **365**, 1282 (2019).
- [15] N. Morali, R. Batabyal, P. K. Nag, E. Liu, Q. Xu, Y. Sun, B. Yan, C. Felser, N. Avraham, and H. Beidenkopf, Fermi-arc diversity on surface terminations of the magnetic weyl semimetal $\text{Co}_3\text{Sn}_2\text{S}_2$, *Science* **365**, 1286 (2019).
- [16] E. Liu, Y. Sun, N. Kumar, L. Muechler, A. Sun, L. Jiao, S.-Y. Yang, D. Liu, A. Liang, Q. Xu, J. Kroder, V. Süß, H. Borrmann, C. Shekhar, Z. Wang, C. Xi, W. Wang, W. Schnelle, S. Wirth, Y. Chen, S. T. B. Goennenwein, and C. Felser, Giant anomalous hall effect in a ferromagnetic kagome-lattice semimetal, *Nature Physics* **14**, 1125 (2018).
- [17] Q. Wang, Y. Xu, R. Lou, Z. Liu, M. Li, Y. Huang, D. Shen, H. Weng, S. Wang, and H. Lei, Large intrinsic anomalous hall effect in half-metallic ferromagnet $\text{Co}_3\text{Sn}_2\text{S}_2$ with magnetic weyl fermions, *Nature Communications* **9**, 3681 (2018).
- [18] G. Li, Q. Xu, W. Shi, C. Fu, L. Jiao, M. E. Kamminga, M. Yu, H. Tüysüz, N. Kumar, V. Süß, R. Saha, A. K. Srivastava, S. Wirth, G. Auffermann, J. Gooth, S. Parkin, Y. Sun, E. Liu, and C. Felser, Surface states in bulk single crystal of topological semimetal $\text{Co}_3\text{Sn}_2\text{S}_2$ toward water oxidation, *Science Advances* **5**, eaaw9867 (2019).
- [19] A. Ozawa and K. Nomura, Two-orbital effective model for magnetic weyl semimetal in kagome-lattice shandite, *Journal of the Physical Society of Japan* **88**, 123703 (2019).
- [20] See Supplemental Material at [URL] for detailed sample preparation, magneto-transport, harmonic Hall technique analysis, spin-torque ferromagnetic resonance analysis, and tight-binding effective-band model calculations.

- [21] I. Belopolski, T. A. Cochran, X. Liu, Z.-J. Cheng, X. P. Yang, Z. Guguchia, S. S. Tsirkin, J.-X. Yin, P. Vir, G. S. Thakur, S. S. Zhang, J. Zhang, K. Kaznatcheev, G. Cheng, G. Chang, D. Multer, N. Shumiya, M. Litskevich, E. Vescovo, T. K. Kim, C. Cacho, N. Yao, C. Felser, T. Neupert, and M. Z. Hasan, Signatures of weyl fermion annihilation in a correlated kagome magnet, *Phys. Rev. Lett.* **127**, 256403 (2021).
- [22] D. F. Liu, Q. N. Xu, E. K. Liu, J. L. Shen, C. C. Le, Y. W. Li, D. Pei, A. J. Liang, P. Dudin, T. K. Kim, C. Cacho, Y. F. Xu, Y. Sun, L. X. Yang, Z. K. Liu, C. Felser, S. S. P. Parkin, and Y. L. Chen, Topological phase transition in a magnetic weyl semimetal, *Phys. Rev. B* **104**, 205140 (2021).
- [23] G. Y. Guo, S. Murakami, T.-W. Chen, and N. Nagaosa, Intrinsic spin hall effect in platinum: First-principles calculations, *Phys. Rev. Lett.* **100**, 096401 (2008).
- [24] A. Hoffmann, Spin hall effects in metals, *IEEE Transactions on Magnetics* **49**, 5172 (2013).
- [25] L. Ye, M. Kang, J. Liu, F. von Cube, C. R. Wicker, T. Suzuki, C. Jozwiak, A. Bostwick, E. Rotenberg, D. C. Bell, L. Fu, R. Comin, and J. G. Checkelsky, Massive dirac fermions in a ferromagnetic kagome metal, *Nature* **555**, 638 (2018).
- [26] K. Fujiwara, J. Ikeda, J. Shiogai, T. Seki, K. Takanashi, and A. Tsukazaki, Ferromagnetic co3sn2s2 thin films fabricated by co-sputtering, *Japanese Journal of Applied Physics* **58**, 050912 (2019).
- [27] J. Ikeda, K. Fujiwara, J. Shiogai, T. Seki, K. Nomura, K. Takanashi, and A. Tsukazaki, Critical thickness for the emergence of weyl features in co3sn2s2 thin films, *Communications Materials* **2**, 18 (2021).
- [28] J. Ikeda, K. Fujiwara, J. Shiogai, T. Seki, K. Nomura, K. Takanashi, and A. Tsukazaki, Two-dimensionality of metallic surface conduction in co3sn2s2 thin films, *Communications Physics* **4**, 117 (2021).
- [29] J. Kim, J. Sinha, M. Hayashi, M. Yamanouchi, S. Fukami, T. Suzuki, S. Mitani, and H. Ohno, Layer thickness dependence of the current-induced effective field vector in Ta|CoFeB|MgO , *Nature Materials* **12**, 240 (2012).
- [30] K. Garello, I. M. Miron, C. O. Avci, F. Freimuth, Y. Mokrousov, S. Blügel, S. Auffret, O. Boulle, G. Gaudin, and P. Gambardella, Symmetry and magnitude of spin-orbit torques in ferromagnetic heterostructures, *Nature Nanotechnology* **8**, 587 (2013).
- [31] C. O. Avci, K. Garello, M. Gabureac, A. Ghosh, A. Fuhrer, S. F. Alvarado, and P. Gambardella, Interplay of spin-orbit torque and thermoelectric effects in ferromagnet/normal-metal bilayers, *Physical Review B* **90**, 224427 (2014).
- [32] N. Roschewsky, E. S. Walker, P. Gowtham, S. Muschinske, F. Hellman, S. R. Bank, and S. Salahuddin, Spin-orbit torque and nernst effect in bi-sb/co heterostructures, *Phys. Rev. B* **99**, 195103 (2019).
- [33] Z. Chi, Y.-C. Lau, X. Xu, T. Ohkubo, K. Hono, and M. Hayashi, The spin hall effect of bi-sb alloy driven by thermally excited dirac-like electrons, *Science Advances* **6**, eaay2324 (2020).
- [34] K. Tang, Z. Wen, Y.-C. Lau, H. Sukegawa, T. Seki, and S. Mitani, Magnetization switching induced by spin-orbit torque from co2mnga magnetic weyl semimetal thin films, *Applied Physics Letters* **118**, 062402 (2021).
- [35] L. Liu, T. Moriyama, D. C. Ralph, and R. A. Buhrman, Spin-torque ferromagnetic resonance induced by the spin Hall effect, *Physical Review Letters* **106**, 036601 (2011).
- [36] J. Shen, Q. Yao, Q. Zeng, H. Sun, X. Xi, G. Wu, W. Wang, B. Shen, Q. Liu, and E. Liu, Local disorder-induced elevation of intrinsic anomalous hall conductance in an electron-doped magnetic weyl semimetal, *Phys. Rev. Lett.* **125**, 086602 (2020).
- [37] I. Belopolski, K. Manna, D. S. Sanchez, G. Chang, B. Ernst, J. Yin, S. S. Zhang, T. Cochran, N. Shumiya, H. Zheng, B. Singh, G. Bian, D. Multer, M. Litskevich, X. Zhou, S.-M. Huang, B. Wang, T.-R. Chang, S.-Y. Xu, A. Bansil, C. Felser, H. Lin, and M. Z. Hasan, Discovery of topological weyl fermion lines and drumhead surface states in a room temperature magnet, *Science* **365**, 1278 (2019).
- [38] K. Manna, L. Muechler, T.-H. Kao, R. Stinchhoff, Y. Zhang, J. Gooth, N. Kumar, G. Kreiner, K. Koepf, R. Car, J. Kübler, G. H. Fecher, C. Shekhar, Y. Sun, and C. Felser, From colossal to zero: Controlling the anomalous hall effect in magnetic heusler compounds via berry curvature design, *Phys. Rev. X* **8**, 041045 (2018).
- [39] A. Markou, J. Gayles, E. Derunova, P. Swekis, J. Noky, L. Zhang, M. N. Ali, Y. Sun, and C. Felser, Hard magnet topological semimetals in xpt3 compounds with the harmony of berry curvature, *Communications Physics* **4**, 104 (2021).
- [40] A. Sakai, S. Minami, T. Koretsune, T. Chen, T. Higo, Y. Wang, T. Nomoto, M. Hirayama, S. Miwa, D. Nishio-Hamane, F. Ishii, R. Arita, and S. Nakatsuji, Iron-based binary ferromagnets for transverse thermoelectric conversion, *Nature* **581**, 53 (2020).
- [41] T. Asaba, V. Ivanov, S. M. Thomas, S. Y. Savrasov, J. D. Thompson, E. D. Bauer, and F. Ronning, Colossal anomalous nernst effect in a correlated noncentrosymmetric kagome ferromagnet, *Science Advances* **7**, eabf1467 (2021).
- [42] Y. Pan, C. Le, B. He, S. J. Watzman, M. Yao, J. Gooth, J. P. Heremans, Y. Sun, and C. Felser, Giant anomalous nernst signal in the antiferromagnet ybmnbi2 , *Nature Materials* **21**, 203 (2022).
- [43] S. Meyer, Y.-T. Chen, S. Wimmer, M. Althammer, T. Wimmer, R. Schlitz, S. Geprägs, H. Huebl, D. Ködderitzsch, H. Ebert, G. E. W. Bauer, R. Gross, and S. T. B. Goennenwein, Observation of the spin nernst effect, *Nature Materials* **16**, 977 (2017).
- [44] P. Sheng, Y. Sakuraba, Y.-C. Lau, S. Takahashi, S. Mitani, and M. Hayashi, The spin nernst effect in tungsten, *Science Advances* **3**, e1701503 (2017).
- [45] Y. Pu, D. Chiba, F. Matsukura, H. Ohno, and J. Shi, Mott relation for anomalous hall and nernst effects in $\text{ga}_{1-x}\text{mn}_x\text{As}$ ferromagnetic semiconductors, *Phys. Rev. Lett.* **101**, 117208 (2008).